

# GAUSS: Guided Encoder - Decoder Architecture for Hyperspectral Unmixing with Spatial Smoothness

D.Y.L. Ranasinghe, H.M.H.K. Weerasooriya, G.M.R.I. Godaliyadda, *Senior Member, IEEE*,  
M.P.B. Ekanayake, *Senior Member, IEEE*, H.M.V.R. Herath, *Senior Member, IEEE*, D. Jayasundara, L. Ramanayake,  
N. Senarath and D. Wickramasinghe

**Abstract**—In recent hyperspectral unmixing (HU) literature, the application of deep learning (DL) has become more prominent, especially with the autoencoder (AE) architecture. We propose a split architecture and use a pseudo-ground truth for abundances to guide the ‘unmixing network’ (UN) optimization. Preceding the UN, an ‘approximation network’ (AN) is proposed, which will improve the association between the centre pixel and its neighbourhood. Hence, it will accentuate spatial correlation in the abundances as its output is the input to the UN and the reference for the ‘mixing network’ (MN). In the Guided Encoder-Decoder Architecture for Hyperspectral Unmixing with Spatial Smoothness (GAUSS), we proposed using one-hot encoded abundances as the pseudo-ground truth to guide the UN; computed using the k-means algorithm to exclude the use of prior HU methods. Furthermore, we release the single-layer constraint on MN by introducing the UN generated abundances in contrast to the standard AE for HU. Secondly, we experimented with two modifications on the pre-trained network using the GAUSS method. In GAUSS<sub>blind</sub>, we have concatenated the UN and the MN to back-propagate the reconstruction error gradients to the encoder. Then, in the GAUSS<sub>prime</sub>, abundance results of a signal processing (SP) method with reliable abundance results were used as the pseudo-ground truth with the GAUSS architecture. According to quantitative and graphical results for four experimental datasets, the three architectures either transcended or equated the performance of existing HU algorithms from both DL and SP domains.

**Index Terms**—Hyperspectral unmixing, deep autoencoder, split architecture, spatial smoothness and correlation, supervised learning

## I. INTRODUCTION

Hyperspectral (HS) imaging is extensively used in earth observation satellites for various applications [1]: lithological mapping [2]–[6], environmental monitoring [7]–[9], and agricultural activities [10]–[12], since it captures more spectral information than its counterparts: multispectral and RGB imaging. However, HS images (HSIs) are of poor spatial resolution and are corrupted by noise and interference from atmospheric alterations and instrumentation imperfections [13]. Therefore, identifying the composition of a topography requires information recovery algorithms, known as unmixing algorithms.

D.Y.L. Ranasinghe, H.M.H.K. Weerasooriya, G.M.R.I. Godaliyadda, H.M.V.R. Herath, M.P.B. Ekanayake, D. Jayasundara, L. Ramanayake, N. Senarath and D. Wickramasinghe are with the Department of Electrical and Electronic Engineering, University of Peradeniya, KY 20400, Sri Lanka (email: e14273@eng.pdn.ac.lk, kavingaweerasooriya@eng.pdn.ac.lk, roshang-odd@ee.pdn.ac.lk, vijitha@eng.pdn.ac.lk, mpb.ekanayake@ee.pdn.ac.lk, e15157@eng.pdn.ac.lk, lakshitharamanayake@eng.pdn.ac.lk, neranjanse-narath95@eng.pdn.ac.lk and dulanhawickramasinghe001@eng.pdn.ac.lk).

HS unmixing (HU) is a source separation technique that strives to extract the constituent source signal spectra and estimate their fractional presence in each pixel, referred to as endmembers and abundances. Over the evolution of HU techniques, numerous unmixing algorithms have been proposed for both linear and non-linear mixing models [14]–[17] under signal processing (SP) and deep learning (DL) domains. SP unmixing benefits from various algorithmic approaches [18] such as geometric [19]–[27], statistical [28]–[30], and sparse regression-based [31], [32]. In addition, non-negative matrix factorization (NMF) [33] has been profoundly used in HU for its concurrent extraction of endmembers and abundances with matrix decomposition and its adherence to fundamental constraints of the HU problem imposed by practical realities such having non-negative abundances. Variants of the NMF algorithm are present in the literature, which promote sparsity of the abundance [34], [35], independence of the endmembers [36], spatial-spectral information and piece-wise smoothness [37]–[40]. Moreover, SP methods are also incorporated with DL unmixing algorithms as initialization methods and supervisory inputs.

Application of DL, though nascent, is now prominent in HU due to the growing capacity in computational power, the ability to incorporate any contextual feature readily and the potentiality to extract information from unstructured data [41]. DL unmixing is frequently performed through semi-supervised or unsupervised fashion using convolutional networks [42]–[49], dense networks [50], [50]–[54], and recurrent networks [55] with the assistance of other functional layers such as pooling, regularization, and shaping. Nonetheless, most DL unmixing algorithms are structured as autoencoders (AEs) due to their resemblance to matrix decomposition applied in blind source separation techniques and their unsupervised learning capabilities.

However, AEs have limitations on the architecture when used for blind unmixing, even though AEs are widely employed in DL unmixing. In particular,

- The encoder optimization is conditioned on the decoder optimization with the end-to-end structure.
- The convergence of the encoder is slower due to the absence of a direct steering mechanism than the decoder because of vanishing gradients.

Besides, according to the ablation studies in [42], [45], [56],

- The convolutional layers distil abstract spatial patterns of

the HSI into the abundance maps rather than learning the association amongst the pixels.

- There is no forcing mechanism to support the spatial correlation in abundance values since the reference for the loss function is the original HSI.

Further, with the end-to-end architecture of AE for blind unmixing,

- The decoder should be limited to a single layer network with linear activations to ensure the resemblance to matrix decomposition [57], [58].
- The non-linearity in spectral information is modelled [55], [59], [60], rather than a non-linear mixing process.

In this regard, we propose the three-network HU architecture (HUA). In the ‘Guided Encoder-Decoder Architecture for Hyperspectral Unmixing with Spatial Smoothness’ (GAUSS) architecture, the first two networks: ‘approximation network’ (AN) and ‘unmixing network’ (UN), constitute the encoder, and the ‘mixing network’ (MN) is the final network that serves as the decoder of the HUA. The AN is introduced to improve the association between the centre pixel and its neighbourhood to improve spatial correlation in abundance. This estimated centre pixel is fed to the UN and used as the output reference for the MN reconstruction error. To ensure the convergence of the AN, the output of that is compared against the spectral signatures of the centre pixel.

Next, we investigate using a pseudo-ground truth, created by first segmenting the HSI with k-means and then converting it to the one-hot encoded representation for abundances to optimize the unmixing process of the spectral signatures. The pseudo-ground truth provides gradients for the UN to optimize its weights untied from the decoder gradients as opposed to conventional optimization of the unmixing process of AEs, where the unmixing optimization is conditioned on the HS pixel or image reconstruction. Besides, the pseudo-ground truth steers the output of the UN towards the latent space spanned by the actual abundances. In addition, we investigate two variants of the HUA to improve its performance. First, inspired by [44], the untied MN will be merged with the UN in the GAUSS<sub>blind</sub> method, while allowing the training only of the encoder to optimize abundances. Further, the merging of the UN and the MN allowed the exclusion of the pseudo-ground truth. Then, in the third method, GAUSS<sub>prime</sub>, the original GAUSS architecture is kept intact while being retrained with a more refined pseudo-ground truth generated by a specifically selected SP algorithm [34] based on its unmixing performance.

Lastly, we address the single-layer constraint present on the MN, which constitutes the decoder, of the typical AE architectures used in existing methods for HU. Because of the use of a pseudo-ground truth to train the UN prior to the training of the MN, the output of the UN is ensured to be at least an approximate abundance of the corresponding pixel. As the UN output is given as the input to the MN and its output is the reconstructed pixel, the decoder requirement is finding the weights that will generate the corresponding spectral signature given an abundance vector. Therefore, because of this explicit nature of the input in the proposed architectures, the decoder

needs not to be confined to a single layer. Thereby, with the design flexibility of the decoder, it is possible to model non-linear mixing for remote sensing through the proposed model.

In summary, the primary contribution of this article is fivefold.

- 1) Introduction of a novel architecture enabling preservation of the smoothness and spatial correlation of the local subspace structure and improving the neighbouring pixels’ association with the centre pixel.
- 2) Introduction of a pseudo-ground truth at the end of an encoder decouples the dependency of the abundance map from the decoder optimization process, enabling the unmixing network to find the solution space independently.
- 3) Introduction of the pseudo-ground truth mechanism enables greater flexibility for the decoder structure and multiple opportunities for subsequent abundance generation steering through refined pseudo-ground truths.
- 4) While expediting the convergence, the guided latent feature space extraction process drives the network’s learning process to a relatively optimum solution. It restrains the solution space and enables the injection of a more refined pseudo-ground truth at subsequent training rounds for further refinement or steering of the unmixing solution.
- 5) This architecture can model the non-linearity of the underlying mixing process as multiple non-linear layers can be stacked to form the decoder.

Further, expanding on the capabilities of the original GAUSS algorithm, we proposed two variants: GAUSS<sub>blind</sub> and GAUSS<sub>prime</sub>, with modifications to the architecture in the former and to the pseudo-ground truth in the latter as a result of the flexibility allowed by the original architecture. Also, the introduction of the three variants established a framework to interpret variances in unmixing performances of different HU algorithms for various HS datasets. The remainder of the paper is as follows. In Section II, the concept of the GAUSS is delineated followed by Section III with implementation details for the HUA. Finally, the experiments and the result comparison with state-of-the-art algorithms are presented in Section IV with explanations for the exceptional performance of the two variants ascribing to the flexibility offered by GAUSS and effective combination of different strategies for a multitude of datasets.

## II. PROBLEM FORMULATION AND THE PRINCIPLES OF THE SOLUTION

### A. Notation

Scalars are denoted by both lower ( $x$ ) and uppercase ( $X$ ) normal fonts. Boldface lowercase fonts ( $\mathbf{x}$ ) are for 1-D arrays, and 1-D arrays are ordered as column vectors. Then, boldface uppercase fonts ( $\mathbf{X}$ ) are for both 2-D and 3-D arrays.

Consider a HSI,  $\mathbf{H} \in \mathbb{R}_+^{w \times h \times B}$ , with a width and a height of  $w$  and  $h$  in pixels, respectively, and  $B$  spectral bands. The HS datacube can be rearranged as a matrix of size  $B \times N$ , where  $N$  is the total number of observations (pixels) and is the product of  $w$  and  $h$ . Accordingly, the HSI can be denoted as  $\mathbf{Y} = [\mathbf{y}_1 \cdots \mathbf{y}_j \cdots \mathbf{y}_N] \in \mathbb{R}_+^{B \times N}$  and each column  $\mathbf{y}_j \in \mathbb{R}_+^B$  is the spectrum of the  $j^{\text{th}}$  pixel. The spectral signature of the pixel at the  $(m, n)$  location of  $\mathbf{H}$  corresponds to the  $j^{\text{th}}$  column vector

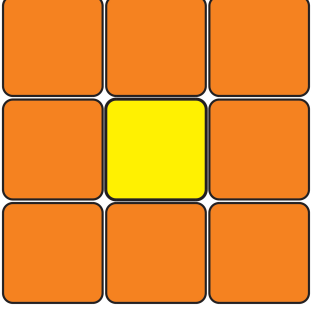


Fig. 1: Moore neighbourhood graph for the approximation network where the centre pixel is in yellow and its neighbourhood in orange

of  $\mathbf{Y}$ , such that  $j = \{w(m-1) + n \mid 1 < m \leq h, 1 < n \leq w\}$  where  $m$  and  $n$  is the row and column position of the pixel, respectively.

### B. Mixture Models

The linear mixture model (LMM) depends on the assumption that the incident light is reflected from the macroscopic surface only once and is measured by the sensing device of the imaging spectrometer without scattering. For its simplicity, LMM is the most frequently used model for HU in the literature [14]. The luxury of the LMM is that a linear combination of endmember spectra can be written for each observation as

$$\mathbf{y}_j = \sum_{k=1}^K \mathbf{S}_{kj} \mathbf{a}_k + \mathbf{e}_j \quad (1)$$

where  $\mathbf{S}_{kj}$  is the fractional composition of the  $k^{\text{th}}$  endmember in the  $j^{\text{th}}$ ,  $\mathbf{a}_k \in \mathbb{R}_+^B$  is the spectrum of the  $k^{\text{th}}$  endmember of the HSI,  $\mathbf{e}_j \in \mathbb{R}_+^B$  is an additive disruption due to noise and modeling errors, and  $K$  is the predetermined number of endmembers in the HSI. The elements in  $\mathbf{y}_j$  and  $\mathbf{a}_k$  are non-negative as the HSI is represented using the reflectance values because it inherits atmospheric corrections and sensor independencies. Due to physical implications, the abundance non-negativity constraint (ANC)  $\mathbf{S}_{kj} \geq 0$  and the abundance sum-to-one constraint (ASC)  $\sum_{k=1}^K \mathbf{S}_{kj} = 1$  are imposed in 1 to assure that the fractional compositions are non-negative and the HSI only consists of the predetermined endmembers. Under the LMM, the HSI can be represented using the matrix notation as

$$\mathbf{Y} = \mathbf{A} \times \mathbf{S} + \mathbf{E} \quad (2)$$

where  $\mathbf{A} \in \mathbb{R}_+^{B \times K}$  is the endmember matrix whose columns are the spectra of each of the  $K$  endmembers,  $\mathbf{S} \in \mathbb{R}_+^{K \times N}$  is the abundance matrix with the fractional composition of each of the  $N$  pixels is organized as a column vector, and  $\mathbf{E} \in \mathbb{R}^{B \times N}$  is the noise matrix. Accordingly, the extraction of the endmember spectra ( $\mathbf{A}$ ) and their abundances ( $\mathbf{S}$ ) are the functions of HU.

When the assumptions of the LMM cannot be satisfied, a non-linear interaction between the signatures will occur. Several

models have been introduced to capture the non-linear behaviour of the mixing process [61]. Intimate mixtures exploit the fact that various particles are in very close vicinity; hence, non-linear interactions between the constituents at microscopic and macroscopic levels. Due to the multipath and scattering, interactions of the photons from different sources give rise to non-linearity. Bi-linear mixture models such non-linear interactions considering that order of interactions is two. Moreover, polynomial mixture models consider the within component interactions as well.

### C. Neighbourhood approximation

While the endmember spectra contain information about the spectral response of the underlying materials in the HSI, the spatial attributes of that image are stored in the abundance matrix. Therefore, in literature, to increase spatial smoothness and spatial correlation of the fractional composition, several regularization functions have been introduced in the objective function [34], [35], [37]–[40] to optimize HU. However, given that the spectral signature of a given HSI is the product of the endmember spectra and its fractional abundances, the spatial correlation and smoothness could be increased using the spectral signatures of the neighbouring pixels.

If the centre pixel can be approximated from its immediate neighbourhood, then the spatial correlation and smoothness shall be established in spectral signatures, thereby in abundance values. Consider the pixel at the  $(m, n)$  location of the HSI ( $\mathbf{H}$ ) and the set ( $\mathcal{S}$ ) of immediate neighbourhood pixels as illustrated in Fig. 1. The set can be defined as,  $\mathcal{S} = \{\mathbf{H}_{i,j} \mid \mathbf{H}_{i,j} \in \mathbb{R}_+^B, i \in \{m-1, m+1\}, j \in \{n-1, n+1\}, i, j \in \mathbb{Z}^+\}$  and the cardinality of the set is equal to the number of neighbourhood pixels considered during the construction of the set and it is denoted by  $|\mathcal{S}|$ .

Then following the pixel to column position transition explained in Section II-A, by rearranging the vectors in  $\mathcal{S}$  as a single column vector denoted by  $\mathbf{n}_j$ , the following relationship can be formulated between the centre pixel ( $\mathbf{y}_j$ ) and its neighbourhood.

$$\mathbf{y}_j \approx \mathbf{W}_n \mathbf{n}_j \quad (3)$$

where  $\mathbf{W}_n \in \mathbb{R}^{B \times B|\mathcal{S}|}$  approximates the centre pixel using its neighbourhood pixel vector  $\mathbf{n}_j$ . To learn the spatial correlation across the HSI,  $\mathbf{W}_n$  can be trained using the following objective function,

$$\arg \min_{\mathbf{W}_n} \|\mathbf{Y} - \mathbf{W}_n \mathbf{N}\|_F^2 \quad (4)$$

Here,  $\mathbf{N}$  is the matrix constructed by concatenating the neighbour vectors of each centre pixel, and  $\mathbf{Y}$  is the matrix form of the HSI and  $\|\cdot\|_F$  is the Frobenius norm. Then by performing HU on pixels generated from the trained  $\mathbf{W}_n$  in (4), the spatial correlation and smoothness could be brought forward to fractional abundances by the AN displayed in Fig. 2.

### D. Controlled abundance estimation

Generally, DL unmixing is performed using the AE architecture with the pixel reconstruction error as the objective function

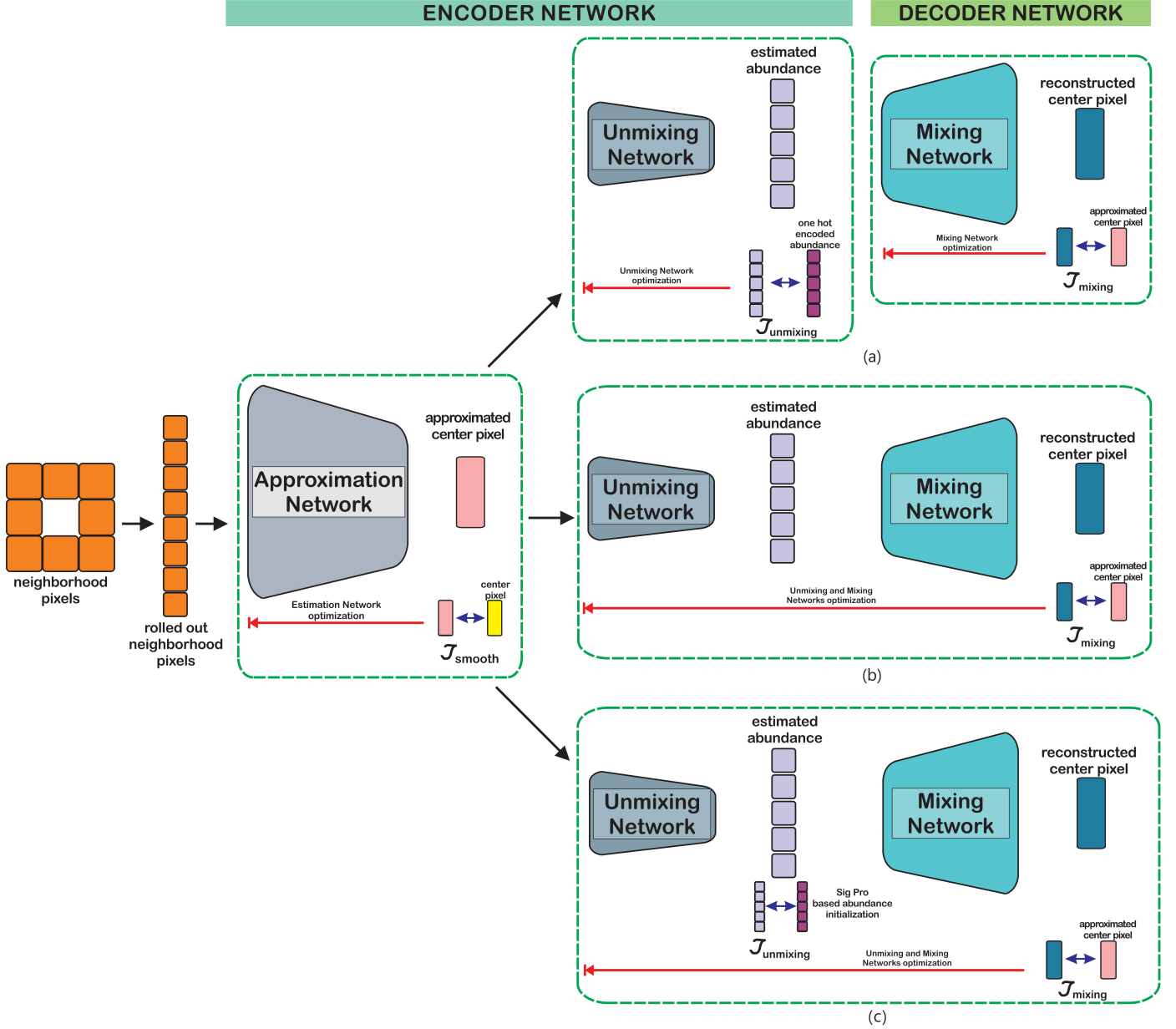


Fig. 2: Proposed GAUSS architectures for hyperspectral unmixing. (a). GAUSS (b). GAUSS<sub>blind</sub> and (c). GAUSS<sub>prime</sub>. The approximation network improves the association of the neighbourhood and uses the approximated centre pixel and the actual centre pixel to compute  $\mathcal{J}_{smooth}$  for optimization. The unmixing network produces the abundances of the smoothed pixels and is optimized by the  $\mathcal{J}_{unmixing}$  which compares the estimated abundances with the pseudo-ground truth abundances. The mixing network outputs the reconstructed centre pixels using the abundances generated from the unmixing network, and  $\mathcal{J}_{mixing}$  optimizes the network by comparing the reconstructed pixel to approximated pixel generated by the approximation network.

to optimize. However, a drawback of using the AE for unmixing is that it precludes direct optimization of abundances in contrast to non-DL methods. Moreover, a conventional AE architecture may suffer from the vanishing gradient problem as the network becomes deeper and deeper. That is because gradients descending through back-propagation may exponentially decrease when they reach the layers in the encoder. In addition, the unmixing process is dependent on the decoder performance of the AE because of the back-to-back connection between the encoder

and the decoder.

Consequently, to avoid the dependency on the endmember signature optimization from the abundance optimization, the proposed work considers an additional objective function to train the network for abundance optimization. We create a reference for the abundance maps to train the UN, first by segmenting the HSI with k-means and converting the result to its one-hot encoded representation. This reference for the abundances is referred to as the pseudo-ground truth and is described in



Section III-C. Further, the injection of a pseudo-ground truth facilitated by the split architecture provides a mechanism to reinforce the abundance optimization. It allows for a more refined pseudo-ground truth from unsupervised SP algorithms as proposed in the  $\text{GAUSS}_{\text{prime}}$  variant (see Section III-D) for subsequent training for better accuracy.

Each pixel's fractional abundances can be considered a probability distribution with the ASC and ANC. Each abundance value for the corresponding endmember is the individual probability. This definition allows us to reconsider the unmixing process as a classification using categorical-cross entropy as the objective function. When the UN learns hidden representations of the HSI by mapping the spectral signatures onto the probability space using the pseudo-ground truth, pixels that are not comprised of pure pixels, *i.e.* mixed pixels, will be forced towards a particular endmember. However, since the UN is a transformation on the pixel signature and the signature of a mixed pixel is different from a pure signature, the fractional abundances can be driven towards pure abundances without losing the generalization of the UN. As these two objectives behave as opposite forces, the fractional abundances will be at an equilibrium rather than driven by a single cost function.

#### E. Expanding decoder flexibility

AEs for HU are omnipresent because they resemble the matrix decomposition used in blind source separation. Since the encoder task is designed to transform the pixel or image of the HS dataset into a latent representation, there is no limitation on the number of layers in the encoder. However, unlike the encoder, the decoder of the AE does not emulate a process; instead performs the matrix multiplication between the abundances and endmembers. Therefore, the endmembers of the HS data are extracted by the weights of the decoder. Hence, the decoder architecture is bound to a single layer decoder to ensure the output of the encoder will be the abundances.

By adopting the pseudo-ground truth mechanism, the UN is trained to produce abundance values at its output in our proposed architecture independent of the decoder architectural form. Therefore, since it is guaranteed that the input of the MN is the abundances of the centre pixel, the single-layered decoder constraint can be released without using recurrent layers as in [55]. Because the output of the decoder is compared against the pixel signature, the decoder requirement is to find the optimal combination of weights that will map the abundances to spectral signatures. Further, the decoder can model the non-linear mixing process with the proposed change.

Therefore, in the  $\text{GAUSS}$  architecture, the pixel's neighbourhood is fed to the AN, and its output is compared against the actual centre pixel and the input to the UN. The UN will generate the abundances of the centre pixel at its output which is subsequently used as the input to the MN. After training, endmembers are generated by feeding an identity matrix ( $\mathbf{I} \in \mathbb{R}^{K \times K}$ ) to the MN, which represents pure pixel feeds because, with the modifications to the decoder architecture, the endmembers can no longer be extracted from the weights of the MN.

#### F. Network architecture variants

Using the AN and the pseudo-ground truth mechanism leads to variants in the architecture. As illustrated in Fig. 2, three possible architectures:  $\text{GAUSS}$ ,  $\text{GAUSS}_{\text{blind}}$ , and  $\text{GAUSS}_{\text{prime}}$  are proposed with different alternatives for the pseudo-ground truth and the encoder-decoder training.

### III. METHODOLOGY

This section elaborates the proposed architecture for HU with spatial smoothness. The proposed method is primarily based on the traditional AE model used in standard HU practice under DL. However, the proposed method can be viewed as three separate networks instead of the standard AE model in HU due to the method of training adapted in this work. The architecture of the aggregated network is illustrated in Fig. 2(a). The AN is used to impose spatial smoothness on the HSI as discussed in Section II-C. The network approximates the centre pixels  $\mathbf{Y} \in \mathbb{R}_+^{B \times N}$  using their neighbourhood pixels  $\mathbf{N} \in \mathbb{R}_+^{B|S| \times N}$  given by

$$\hat{\mathbf{Y}} = f_n(\mathbf{N}) \quad (5)$$

with  $f_n: \mathbb{R}_+^{B|S| \times N} \rightarrow \mathbb{R}_+^{B \times N}$ . The network learns the parameters for approximation by minimizing the average reconstruction error between the input  $\mathbf{Y}$  and the reconstructed spectral signatures  $\hat{\mathbf{Y}}$  from the neighbourhood pixels. Therefore, after the learning process is terminated, the smoothness matrix ( $\mathbf{W}_n$ ) in (4) and the spectral signatures with improved spatial characteristics can be realized by

$$\text{Smoothness transitions: } f_n(\mathbf{N}) \Rightarrow \mathbf{W}_n \mathbf{N} \quad (6)$$

$$\text{Smoothed pixels: } \hat{\mathbf{Y}}. \quad (7)$$

Next, to learn the hidden representation of the HSI, the UN is trained, which transforms the smoothed spectral signatures ( $\hat{\mathbf{Y}}$ ) from the AN to a low dimensional representation ( $\hat{\mathbf{L}} \in \mathbb{R}_+^{K \times N}$ ) given by

$$\hat{\mathbf{L}} = f_e(\hat{\mathbf{Y}}), \quad (8)$$

with  $f_e: \mathbb{R}_+^{B \times N} \rightarrow \mathbb{R}_+^{K \times N}$ . The output from the UN is fed to the MN, which decompresses the hidden representation to reconstruct the smoothed spectral signatures at its output. The decoder function, therefore, can be represented as

$$\hat{\mathbf{Y}} = f_d(\hat{\mathbf{L}}) \quad (9)$$

where  $f_d: \mathbb{R}_+^{K \times N} \rightarrow \mathbb{R}_+^{B \times N}$ , and  $\hat{\mathbf{Y}}$  is the output of the decoder network. After the successful termination of the learning process for HU, the unmixing results can be extracted by:

$$\begin{aligned} \text{Abundance estimation: } \hat{\mathbf{L}}^* &\Rightarrow \hat{\mathbf{S}} \\ \text{Endmember estimation: } f_d^*(\mathbf{I}_K) &\Rightarrow \hat{\mathbf{A}} \end{aligned} \quad (10)$$

where  $\mathbf{I}_K \in \mathbb{R}_+^{K \times K}$  is the identity matrix and  $*$  denotes the optimal solution at the end of training process.

### A. Encoder

The encoder combines the AN and UN to improve spatial characteristics and learn hidden representations in this work. For each pixel of the HSI, we first consider its immediate neighbourhood and reconstruct the centre pixel from the set of neighbourhood pixels. Then, the output of the AN is sent to the UN to learn the unmixing process and estimate abundances. The architecture of the encoder is given in Fig. 2(a), and fully connected layer (FCNL) architecture is used in constructing the encoder.

In our work, the fractional abundances are considered probabilities, and learning hidden representations of the HSI is similar to performing a multi-class classification with the pseudo-ground truths. In our work, the encoder is designed to use spatial information and optimize the estimation of fractional abundances without interference from the decoder optimization. To optimize the AN, we use the reconstruction error of the centre pixel from its neighbourhood as given by

$$\mathcal{J}_{\text{smooth}} = \frac{1}{N} \|\mathbf{Y} - \hat{\mathbf{Y}}\|_F^2 \quad (11)$$

where  $\|\cdot\|_F$  is the Frobenius norm. Then, to abide by the ANC and ASC, we apply the following scaling and standardization at the final layer of the UN defined as follows,

$$\hat{l}_{kj} = \frac{e^{-z_{kj}}}{\sum_{k=1}^K e^{-z_{kj}}} \quad (12)$$

where  $z_{kj}$  is the output of the  $k^{\text{th}}$  node at the final layer of the encoder prior activation and  $\hat{l}_{kj}$  is the estimated fractional abundance for the  $k^{\text{th}}$  endmember of the  $j^{\text{th}}$  column in  $\hat{\mathbf{L}}$ . The standardization to probability distributions given in 12 can be realized through *Softmax* activation function of the output layer of the encoder. Then to optimize the unmixing process of the encoder, the categorical cross-entropy is used as below,

$$\mathcal{J}_{\text{unmixing}} = -\frac{1}{N} \sum_{j,k=1}^{N,K} l_{kj} \log \hat{l}_{kj} + (1 - l_{kj}) \log(1 - \hat{l}_{kj}) \quad (13)$$

where  $l_{kj}$  are abundance values for  $k^{\text{th}}$  endmember of the  $j^{\text{th}}$  column of the pseudo-ground truth used to expedite optimization of the UN.

### B. Decoder

An MLP-based network is adopted for the decoder in our proposed scheme, with its structure reported in Fig. 2. In this work, the decoder is designed to reconstruct the input to the UN, which comprises smoothed pixels generated from the AN of the proposed architecture. As discussed in Section III-A, with a pseudo-ground truth mechanism for abundance estimation, the decoder architecture is not restricted to a single-layered linear network; therefore, it can learn non-linear relationships as well.

The decoder of the proposed network learns non-linearity relationships between abundances and endmember signatures during the mixing process because of the introduced extension in the layers. Nevertheless, as mentioned in Section III-B, by

extending the decoder layers, the extraction of the endmember signatures cannot be done through the network weights because the unmixing process is now not limited to a single layer rather laid out over a single network with multiple layers. However, since the decoder is trained by using abundances generated from the encoder network, the decoder can reconstruct the corresponding spectral signature for any abundance vector in the low dimensional space learned by the encoder. Hence, by feeding this one-hot encoded vector to the decoder at the end of weight training, the spectral information of the corresponding endmember can be extracted. For example, to find the endmember signature of the  $k^{\text{th}}$  endmember, we will construct a one-hot vector  $\mathbf{o}_k$  such that  $\mathbf{o}_k = [0, \dots, 0, 1, 0, \dots, 0]$  where the unity entry is at the  $k^{\text{th}}$  position of the vector. The vector format implies the existence of a pure pixel containing only that end member. Hence, the resulted spectral signature of the MN is simply the corresponding endmember signature. Then by concatenating these one-hot vectors of each endmember, we can construct an identity matrix, when given to the decoder, which will output the endmember signatures of the HSI in a single attempt as presented in 10 for endmember estimation.

To train the decoder network, we diverge from the conventional practice of using the mean squared error between the encoder input  $\mathbf{Y}$  and the decoder output of each pixel  $\hat{\mathbf{Y}}$  defined as

$$\mathcal{J}_{\text{reconstruction}} = \frac{1}{NB} \|\mathbf{Y} - \hat{\mathbf{Y}}\|_F^2 \quad (14)$$

for the HSI. Rather, we adopt the pixel spectral information divergence (pSID) proposed by [62] as the reconstruction error to optimize the mixing process, which is defined by,

$$\begin{aligned} \mathcal{J}_{\text{mixing}} &= D(\hat{\mathbf{Y}} \|\hat{\mathbf{Y}}) + D(\hat{\mathbf{Y}} \|\hat{\mathbf{Y}}) \\ &= \frac{1}{N} \sum_{j,b=1}^{N,B} \left\{ q_{bj} \log \left( \frac{q_{bj}}{\hat{q}_{bj}} \right) + \hat{q}_{bj} \log \left( \frac{\hat{q}_{bj}}{q_{bj}} \right) \right\} \end{aligned} \quad (15)$$

where  $\mathbf{q}_j = \hat{\mathbf{y}}_j / \|\hat{\mathbf{y}}_j\|_1$  and  $\hat{\mathbf{q}}_j = \hat{\hat{\mathbf{y}}}_j / \|\hat{\hat{\mathbf{y}}}_j\|_1$  are the probability distribution vectors of the spectral signature of the  $j^{\text{th}}$  pixel of  $\hat{\mathbf{Y}}$  and  $\hat{\mathbf{Y}}$ , respectively. Accordingly,  $q_{bj}$  and  $\hat{q}_{bj}$  represent the probability values of the  $b^{\text{th}}$  band of the  $j^{\text{th}}$  pixel. Then,  $\|\cdot\|_1$  is 1-norm of the corresponding spectral signature. In 15,  $D(\cdot \|\cdot)$  is called the relative entropy between the smoothed pixels at the UN input and reconstructed pixels at the decoder output. The pSID defined by 15 can be used to measure the spectral similarity between corresponding pixel vectors in  $\hat{\mathbf{Y}}$  and  $\hat{\mathbf{Y}}$ .

### C. Pseudo-ground truth preparation for abundances

In the original GAUSS architecture, one-hot encoded representation is used as the pseudo-ground truth to guide the UN of the encoder. To construct the one-hot encoded representation of the HSI, we first segment the HSI using the k-means algorithm on the spectral signatures. Further, injection of the pseudo-ground truth enables greater flexibility for the decoder structure and multiple opportunities for subsequent abundance

generation steering through refined pseudo-ground truths as proposed below.

#### D. Variants of the GAUSS algorithm

The GAUSS architecture is the foundation that uses the one-hot encoder abundances as the pseudo-ground truth. Then, we propose two architecture variants:  $\text{GAUSS}_{\text{blind}}$  and  $\text{GAUSS}_{\text{prime}}$ , for HU that are pre-trained using the GAUSS method. First, following [44], we will connect the decoder to the UN and remove the pseudo-ground truth. Then, we will train the network, similar to the conventional DL unmixing method, without allowing the decoder to train. This strategy will allow the unmixing process to optimize abundance results according to pixel reconstruct error defined by 15. After its completion, the decoder of the HUA will be trained while the encoder training is withheld. For reference, this training method is called ‘ $\text{GAUSS}_{\text{blind}}$ ’ (see Fig. 2(b)).

Second, analogous to using unsupervised HU algorithms for endmember weight initialization, we consider abundance results of a SP algorithm with reliable unmixing performance as a pseudo-ground truth for HUA. This training strategy is referred to as the ‘ $\text{GAUSS}_{\text{prime}}$ ’ method (see Fig. 2(c)). The  $\text{GAUSS}_{\text{prime}}$  method is a combination of both GAUSS and  $\text{GAUSS}_{\text{blind}}$  strategies because and facilitates a hybrid modus operandi by fusing the best of the abilities of the other two methods. However, the output of the UN will be compared against the new pseudo-ground truth. Further, in this scheme, the encoder and the decoder will also be trained successively like in the  $\text{GAUSS}_{\text{blind}}$  strategy. Nonetheless, the subsequent refinement in abundance optimization steering through the insertion of abundance maps generated via high performing SP was enabled by using the pseudo-ground truth mechanism. Accordingly, we use the abundance results of the  $L_{1/2}$  NMF algorithm for all the datasets to maintain consistency even though it could be any contextual driver for abundance generation.

#### E. Implementation and training of the network

The HUA was developed in TensorFlow v2 using the Google Colaboratory using default settings for optimization parameters, and the detailed architecture of the HUA is given in Table I. Then the Adam optimizer was used to optimize the three networks, and for the input-output dataset preparation, we used a batch size of 32 for each HSI dataset.

In all three training strategies, the encoder and the decoder are successively trained, and the section was trained for 25 epochs because the  $\text{GAUSS}_{\text{blind}}$  and  $\text{GAUSS}_{\text{prime}}$  methods are used with the network pre-trained by the GAUSS method. Accordingly, in both  $\text{GAUSS}_{\text{blind}}$  and  $\text{GAUSS}_{\text{prime}}$ , the HUA was first trained for 25 epochs under the GAUSS method, and another 25 epochs either with the  $\text{GAUSS}_{\text{blind}}$  and  $\text{GAUSS}_{\text{prime}}$  method totalled 50 epochs. Since the total number of epochs for the GAUSS method is different from that for the other two methods, the pre-trained AE was further trained for additional 25 epochs with the GAUSS method to enable fair comparison amongst the proposed three algorithms.

The pseudo-ground truth used for the  $\text{GAUSS}_{\text{prime}}$  method was the abundance results from the  $L_{1/2}$  NMF algorithm considering its abundance performance for all three real datasets.

## IV. EXPERIMENTS AND DISCUSSIONS

### A. Performance criteria

The performance of the abundance estimation is measured by the average root mean square error (aRMSE), average abundance information divergence (aAID), and average abundance angle distance (aAAD). Then, the accuracy of endmember estimation from the HU algorithm is evaluated using the average spectral angle distance (aSAD) and the average spectral information divergence (aSID), which are defined as follows,

$$\text{aRMSE} = \sqrt{\frac{1}{NK} \|\mathbf{S} - \hat{\mathbf{S}}\|_F^2} \quad (16)$$

$$\text{aAAD} = \frac{1}{N} \sum_{j=1}^N \cos^{-1} \left( \frac{\langle \mathbf{s}_j, \hat{\mathbf{s}}_j \rangle}{\|\mathbf{s}_j\| \|\hat{\mathbf{s}}_j\|} \right) \quad (17)$$

$$\text{aAID} = \frac{1}{N} \sum_{j=1}^N \sum_{k=1}^K \left\{ s_{kj} \log \left( \frac{s_{kj}}{\hat{s}_{kj}} \right) + \hat{s}_{kj} \log \left( \frac{\hat{s}_{kj}}{s_{kj}} \right) \right\} \quad (18)$$

$$\text{aSAD} = \frac{1}{K} \sum_{k=1}^K \cos^{-1} \left( \frac{\langle \mathbf{a}_k, \hat{\mathbf{a}}_k \rangle}{\|\mathbf{a}_k\| \|\hat{\mathbf{a}}_k\|} \right) \quad (19)$$

$$\text{aSID} = \frac{1}{K} \sum_{k=1}^K \sum_{b=1}^B \left\{ p_{bk} \log \left( \frac{p_{bk}}{\hat{p}_{bk}} \right) + \hat{p}_{bk} \log \left( \frac{\hat{p}_{bk}}{p_{bk}} \right) \right\} \quad (20)$$

where  $\mathbf{S}$  and  $\hat{\mathbf{S}}$  represents the ground truth and estimated abundances. Then,  $\mathbf{s}_j$  and  $\hat{\mathbf{s}}_j$  are the ground truth and estimated abundances at  $j^{\text{th}}$  column or pixel, and  $s_{kj}$  and  $\hat{s}_{kj}$  are the ground truth and estimated abundance value for  $k^{\text{th}}$  endmember of the  $j^{\text{th}}$  pixel. Next,  $\mathbf{a}_k$  and  $\hat{\mathbf{a}}_k$  are ground truth and extracted endmember for the  $k^{\text{th}}$  source, and  $p_{bk}$  and  $\hat{p}_{bk}$  are probability value for the  $b^{\text{th}}$  spectral band of the  $k^{\text{th}}$  ground truth and extracted endmembers, respectively. The probability vector for the  $k^{\text{th}}$  endmember is computed as  $\mathbf{p}_k = \mathbf{a}_k / \|\mathbf{a}_k\|$  and  $\hat{\mathbf{p}}_k = \hat{\mathbf{a}}_k / \|\hat{\mathbf{a}}_k\|$  for the ground truth and extracted signatures, respectively.

### B. Experimental setting

To generate a synthetic image with  $128 \times 128$  of spatial resolution and 480 of spectral resolution, the United States Geological Survey (USGS)<sup>1</sup> endmember library [63] and the

<sup>1</sup><https://www.usgs.gov/labs/spectroscopy-lab/science/spectral-library>

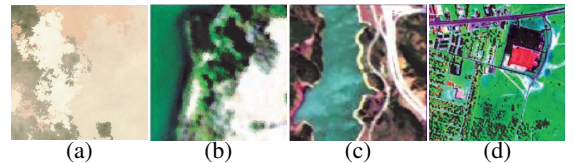


Fig. 3: RGB images of the datasets (a). Simulated (b). Samson (c). Jasper-Ridge (d). Urban

TABLE I  
Network parameters of the autoencoder for unmixing

Network	Layer description	Output shape	Bias state
Encoder	Approximation network	Input layer	[(None, $ S  \times B$ )]
		Dense layer 1	(None, $\lfloor  S  \times B/2 \rfloor$ )
		Dense layer 2	(None, $\lfloor  S  \times B/8 \rfloor$ )
		Dense layer 3	(None, $B$ )
	Unmixing network	Input layer	[(None, $B$ )]
		Dense layer 1	(None, $\lfloor B/2 \rfloor$ )
		Dense layer 2	(None, $\lfloor B/8 \rfloor$ )
Decoder	Unmixing network	Dense layer 3	(None, $K$ )
		Input layer	[(None, $K$ )]
		Dense layer 1	(None, $\lfloor B/4 \rfloor$ )
		Dense layer 2	(None, $B$ )

$\lfloor \cdot \rfloor$  represents the floor operation.

Hyperspectral Imagery Synthesis Toolbox (HSIST)<sup>2</sup> were utilized. However, since these endmembers were acquired under laboratory conditions and HSI is of no noise, the generated image does not resemble an HSI in the wild. Therefore, the following steps were carried out to obtain a dataset more representative of the practical context for comparison purposes. Initially, four endmembers were chosen: "Zircon, Montmorillonite, Lawn grass, and Hypersthene". Next, a 30 dB additive white Gaussian noise (AWGN) was added to each endmember independently. Afterwards, each HS pixel was created linearly using the Spherical Gaussian abundance fields with default parameters. After that, each HS pixel was created with different AWGN noises assuming that noise due to the environmental effects such as interference and scattering is distinct from pixel to pixel. Next, a separate 30 dB additive noise was superimposed on the final HSI to imitate the measurement noise.

Moreover, a set of three real HS datasets<sup>3</sup>: Samson, Jasper-Ridge, and Urban were used for quantitative evaluation purposes. The Samson dataset consists of three endmembers with 156 spectral bands covering 401 nm to 889 nm wavelengths, while Jasper-Ridge comprises four sources with 198 spectral bands ranging from 380 nm to 2500 nm. The urban dataset has 162 spectral bands spanning the region from 400 nm to 2500 nm and five endmembers. The spatial resolutions of the datasets, in units of pixels  $\times$  pixels, are  $95 \times 95$ ,  $100 \times 100$  and  $307 \times 307$ , respectively.

In order to compare the results of the proposed algorithm, we have chosen eight different states of the art algorithms. while CNNAEU [44], DAEN [52], [57], uDAS [51] and EGU-

Net [64] exploits various DL architectures for unmixing.  $L_{1/2}$  NMF [34], R-CoNMF [26], MLNMF [65], SULoRA [66] and VCA-FCLS [19] are the popular examples for signal processing algorithms. These algorithms leverage different NMF and other geometric based frameworks. The proposed and the competitive algorithms were tested on the real hyperspectral datasets as well as the simulated dataset. The RGB images of the datasets are illustrated in Fig. 3.

### C. Experiments on simulated data

When the results of the DL and conventional unmixing are considered whole, the conventional algorithms have surpassed DL unmixing algorithms in the abundance estimation front for the simulated dataset. The conventional unmixing algorithms used in the analysis are geometric methods, and their derivation is based on ideal HSIs. The simulated dataset resonates with the requirement of those algorithms. Additionally, although the noise was added to the simulated dataset, pure or marginally perturbed pixels are still present in the HS dataset, favouring unmixing algorithms that exploit underlying geometric frameworks to prevail over DL unmixing algorithms. Accordingly, we use the  $L_{1/2}$  NMF abundance results to create the pseudo-ground truth for the GAUSS<sub>prime</sub> method to provide a more refined steering mechanism to optimize the abundance outputted from the UN.

The use of the  $L_{1/2}$  NMF abundance results has aided the decoder network in producing the best performance for endmembers surpassing the R-CoNMF algorithm marginally. Notably, the HUA under the GAUSS<sub>prime</sub> training method has managed to be better than its pseudo-ground truth abundances from the  $L_{1/2}$  NMF algorithm and patently every other DL unmixing method used for blind HU. Hence, the result proves the benefit of using supervisory data to train the HUA for HU as the network benefits from both model-based and data-based learning advantages. Further, the superior performance of the GAUSS<sub>prime</sub> method should not foreshadow the fact that the injection of a more refined pseudo-ground truth was enabled by the original mechanism proposed with the GAUSS method.

Besides, in Section IV-B, two noises were added to consider the performance of the HUA in terms of noise suppression and impurity removal of the endmembers, and as presented in Fig. 5, endmembers extracted from the GAUSS<sub>blind</sub> and GAUSS<sub>prime</sub> methods have no visible deviation from the endmember ground truths. Though neural networks are less prone to noise, the removal of endmember unique noise and image noise could be ascribed to the network's AN. Since the AN of the HUA enhances the association between the centre pixel and its neighbourhood, the network attempts to represent the centre pixel as a combination of the neighbourhood pixels. Since endmember impurities are unique to the pixel, to approximate the centre pixel, the network should learn the overlapping or the correlated effect from the endmembers, thereby minimizing the effect of pixel unique impurities. Since this output is used as the reference for the decoder output, the decoder network will attempt to learn the endmembers excluding pixel unique impurities. Hence, as evident from the Table II, the improvements in the unmixing

<sup>2</sup>[http://www.ehu.eus/ccwintco/index.php/Hyperspectral\\_Imagery\\_Synthesis\\_tools\\_for\\_MATLAB](http://www.ehu.eus/ccwintco/index.php/Hyperspectral_Imagery_Synthesis_tools_for_MATLAB)

<sup>3</sup><https://rslab.ut.ac.ir/data>

TABLE II

Unmixing performance comparison for the four datasets: Simulated, Samson, Jasper-ridge, and Urban. The best performing algorithms are ranked up to the third, and the ranks are superscript.

		Proposed methods			Deep learning methods					Signal processing methods				
		GAUSS	GAUSS <sub>blind</sub>	GAUSS <sub>prime</sub>	CNNAEU	DAEN	DAEU	EGU <sub>net</sub>	uDAS	$L_{1/2}$ NMF	R-CoNMF	MLNMF	SULoRA	VCA FCLS
Simulated	aRMSE	0.1816	0.0134	0.0090 <sup>3</sup>	0.1316	0.2292	0.1160	0.0155	0.0122	0.0259	0.0064 <sup>1</sup>	0.0553	0.0124	0.0078 <sup>2</sup>
	aAAD	2.8140	0.0096	0.0044 <sup>3</sup>	0.7059	1.2246	1.5834	0.0076	0.0081	0.0293	0.0023 <sup>1</sup>	0.0774	0.0085	0.0035 <sup>2</sup>
	aAID	0.2638	0.0315	0.0203 <sup>3</sup>	0.2400	0.5843	0.2135	0.0320	0.0284	0.0643	0.0152 <sup>1</sup>	0.1218	0.0289	0.0185 <sup>2</sup>
	aSAD	0.0775	0.0002 <sup>3</sup>	0.0002 <sup>1</sup>	0.0104	0.0071	0.0265	0.0071	0.0002	0.0002	0.0002 <sup>2</sup>	0.0002	0.0002	0.0002
	aSID	0.1327	0.0041	0.0029 <sup>1</sup>	0.0559	0.0390	0.0905	0.0322	0.0050	0.0051	0.0030 <sup>2</sup>	0.0035 <sup>3</sup>	0.0050	0.0050
Samson	aRMSE	0.1945	0.1340 <sup>3</sup>	0.0441 <sup>1</sup>	0.2331	0.3122	0.1202 <sup>2</sup>	0.1860	0.3115	0.1682	0.3116	0.1585	0.2214	0.2769
	aAAD	1.1887	0.3906 <sup>2</sup>	0.0646 <sup>1</sup>	1.7412	2.9078	0.7953	0.7318	3.1019	0.5919 <sup>3</sup>	3.4247	0.7035	1.3849	2.7987
	aAID	0.2457	0.1840 <sup>3</sup>	0.0634 <sup>1</sup>	0.3821	0.5949	0.1747 <sup>2</sup>	0.3260	0.6063	0.2426	0.6068	0.2557	0.3367	0.5144
	aSAD	0.0589	0.0320	0.0166 <sup>2</sup>	0.0233	0.2637	0.0069 <sup>1</sup>	0.1604	0.0282	0.0233	0.0237	0.0249	0.0250	0.0226 <sup>3</sup>
	aSID	0.1041	0.1126	0.0535 <sup>2</sup>	0.0615 <sup>3</sup>	0.1605	0.0462 <sup>1</sup>	0.2619	0.0724	0.0690	0.0727	0.0676	0.0801	0.0666
Jasper-ridge	aRMSE	0.1446	0.1024 <sup>2</sup>	0.0456 <sup>1</sup>	0.1621	0.1567	0.1496	0.1174	0.1783	0.1647	0.1552	0.1150	0.1058 <sup>3</sup>	0.2069
	aAAD	0.5920 <sup>2</sup>	0.6574 <sup>3</sup>	0.1375 <sup>1</sup>	1.3699	1.5099	1.1180	0.8785	1.0615	1.3408	1.4804	0.9288	0.7006	1.8704
	aAID	0.2382	0.1822 <sup>2</sup>	0.0817 <sup>1</sup>	0.3016	0.2997	0.2550	0.2163	0.2971	0.3692	0.2992	0.2070	0.1878 <sup>3</sup>	0.3990
	aSAD	0.0149 <sup>1</sup>	0.0319	0.0347	0.2784	0.7825	0.0182 <sup>2</sup>	0.1947	0.0312 <sup>3</sup>	0.2060	0.0414	0.1924	0.1966	0.2074
	aSID	0.0833 <sup>1</sup>	0.1195 <sup>3</sup>	0.1203	0.2495	0.3175	0.0853 <sup>2</sup>	0.2997	0.1263	0.2118	0.1377	0.2049	0.2897	0.3179
Urban	aRMSE	0.1358	0.0868 <sup>1</sup>	0.1857	0.0933 <sup>2</sup>	0.2612	0.1925	0.1210 <sup>3</sup>	0.2236	0.2871	0.2415	0.2722	0.2633	0.3416
	aAAD	0.6830 <sup>2</sup>	0.5657 <sup>1</sup>	2.6524	0.9254 <sup>3</sup>	5.1605	3.3683	1.4179	3.5392	4.0281	4.6971	4.3343	3.7239	9.5600
	aAID	0.2613 <sup>3</sup>	0.1823 <sup>1</sup>	0.5050	0.2127 <sup>2</sup>	0.7775	0.4429	0.2678	0.6011	0.7656	0.6716	0.7913	0.7326	0.9966
	aSAD	0.0059 <sup>3</sup>	0.0035 <sup>1</sup>	0.5316	0.0064	0.6125	0.0685	0.0040 <sup>2</sup>	1.2614	1.0874	0.8814	0.6390	1.2024	1.1611
	aSID	0.0654	0.0181 <sup>1</sup>	0.3378	0.0544 <sup>3</sup>	0.5055	0.1702	0.0351 <sup>2</sup>	0.3694	0.5068	0.3477	0.5167	0.4956	0.5005

performance of the GAUSS<sub>prime</sub> method and the endmember extraction performance of the GAUSS<sub>blind</sub> method have been facilitated by the originally proposed mechanisms of the GAUSS architecture

The poor performance of the GAUSS method is due to its failure to unmix the very minute differences in the abundances. As given in Fig. 6, each histogram of the abundances has two modes, and the lower abundance values are approximately centred around 0.1. In comparison, the higher abundances values are centred around 0.7. This apparent bi-modality in the histogram explains the binarization of the abundance maps under the GAUSS method. Furthermore, since there is no sufficient count of pure abundances, the pseudo-ground truth created using the k-means algorithm does not span the entire actual abundances or latent space, rather a subspace of it where most abundances are on the vertices of that subspace. Consequently, even at its optimal point, the decoder will produce a combination of the pure endmembers, and this result is illustrated in Fig. 5. In Fig. 5, the extracted endmembers for the GAUSS method diverge from the actual endmembers compared to the results of the other two methods. Nonetheless, the GAUSS<sub>blind</sub> and GAUSS<sub>prime</sub> methods have righted the errors in the GAUSS method. The results have improved significantly from the GAUSS to GAUSS<sub>blind</sub> method, especially concerning endmember extraction. Therefore, even though the binarization in the GAUSS method hindered its performance, it has aided the optimization of the networks in the GAUSS<sub>blind</sub> method. Its performance has come between the best three performers for DL methods.

#### D. Experiments on real data

1) *Samson dataset*: It is imperative to understand the Samson dataset to analyze the performance of the three methods. It has three principal endmembers, and the boundaries of these endmembers are almost non-overlapping. Hence, the Samson dataset can be considered a sparse-abundance image similar to the simulated dataset. Though the GAUSS method has not produced competitive quantitative results, it can be observed from Fig. 4 that the proposed method has been able to identify the boundary of each endmember. Furthermore, the high performance of the GAUSS<sub>blind</sub> and the GAUSS<sub>prime</sub> suggests that the one-hot encoded maps have been insufficient in steering the abundance optimization for the GAUSS method and highlights the importance of using  $L_{1/2}$  NMF abundances and combined training with the other two architectures. This speculation is corroborated by the water endmember results in Fig. 5 because a mixed endmember has been captured with the GAUSS compared to the other two methods. Also, if we remove the GAUSS<sub>blind</sub> and GAUSS<sub>prime</sub> methods from the comparison, the GAUSS method still produces competitive results for abundance and would have the third-best performance for aAID. Consequently, the pre-training of the HUA under the GAUSS method has driven the optimization towards an optimal solution space that further optimized the reconstruction error gradients.

Next, the GAUSS<sub>prime</sub> has performed best in terms of abundance estimation with the aid of the  $L_{1/2}$  NMF algorithm that enabled further steering. According to Table II, the  $L_{1/2}$  NMF algorithm has better results than the GAUSS method and has come close to the GAUSS<sub>blind</sub> results. Furthermore, from the  $L_{1/2}$  NMF abundance maps in Fig. 4, it can be seen that there is more smoothness in the abundances compared to the abundance



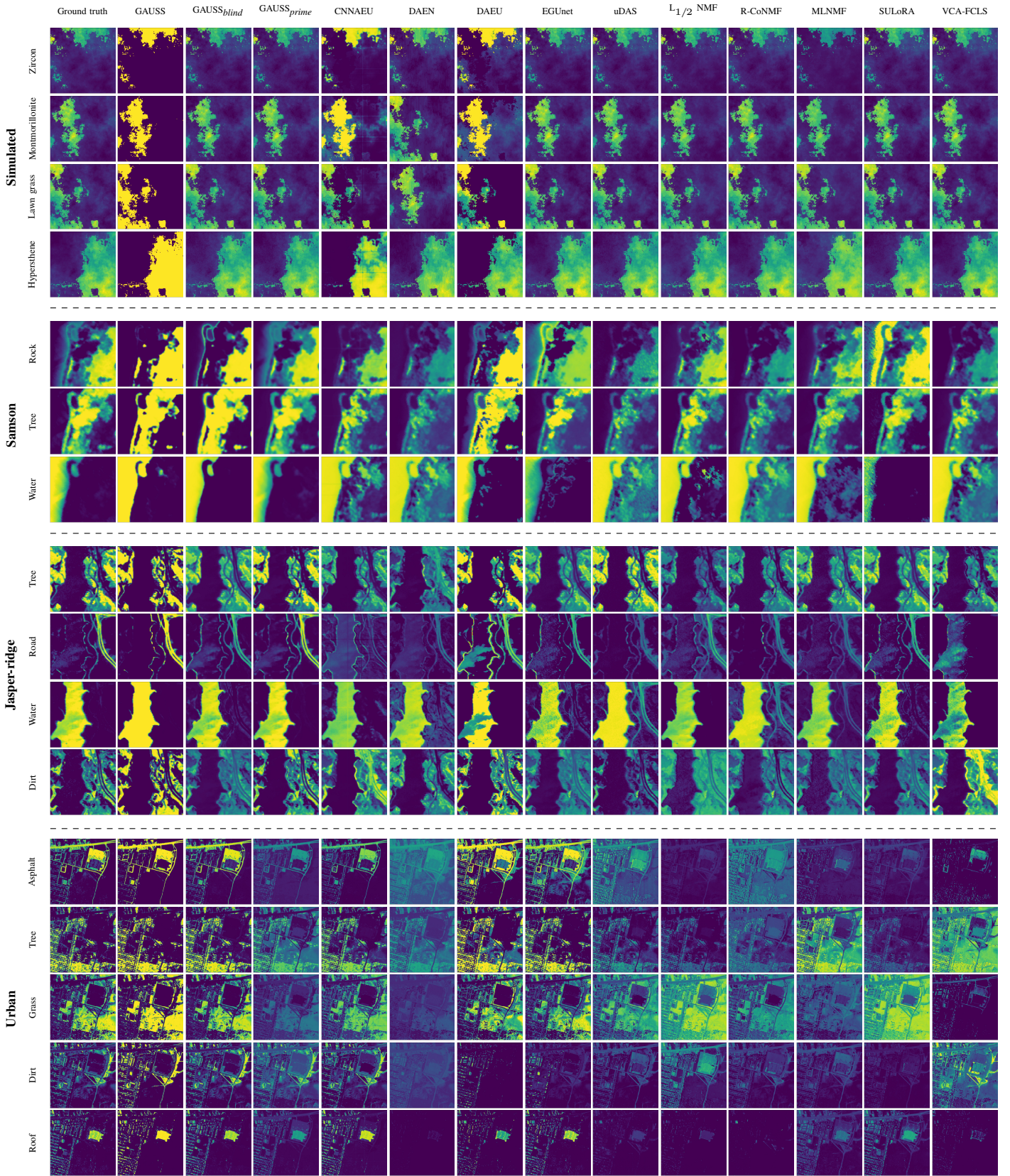


Fig. 4: Abundance map for the Simulated, Samson, Jasper-ridge, and Urban datasets for the proposed GAUSS, GAUSS<sub>blind</sub>, and GAUSS<sub>prime</sub> methods with the results for the comparison algorithms

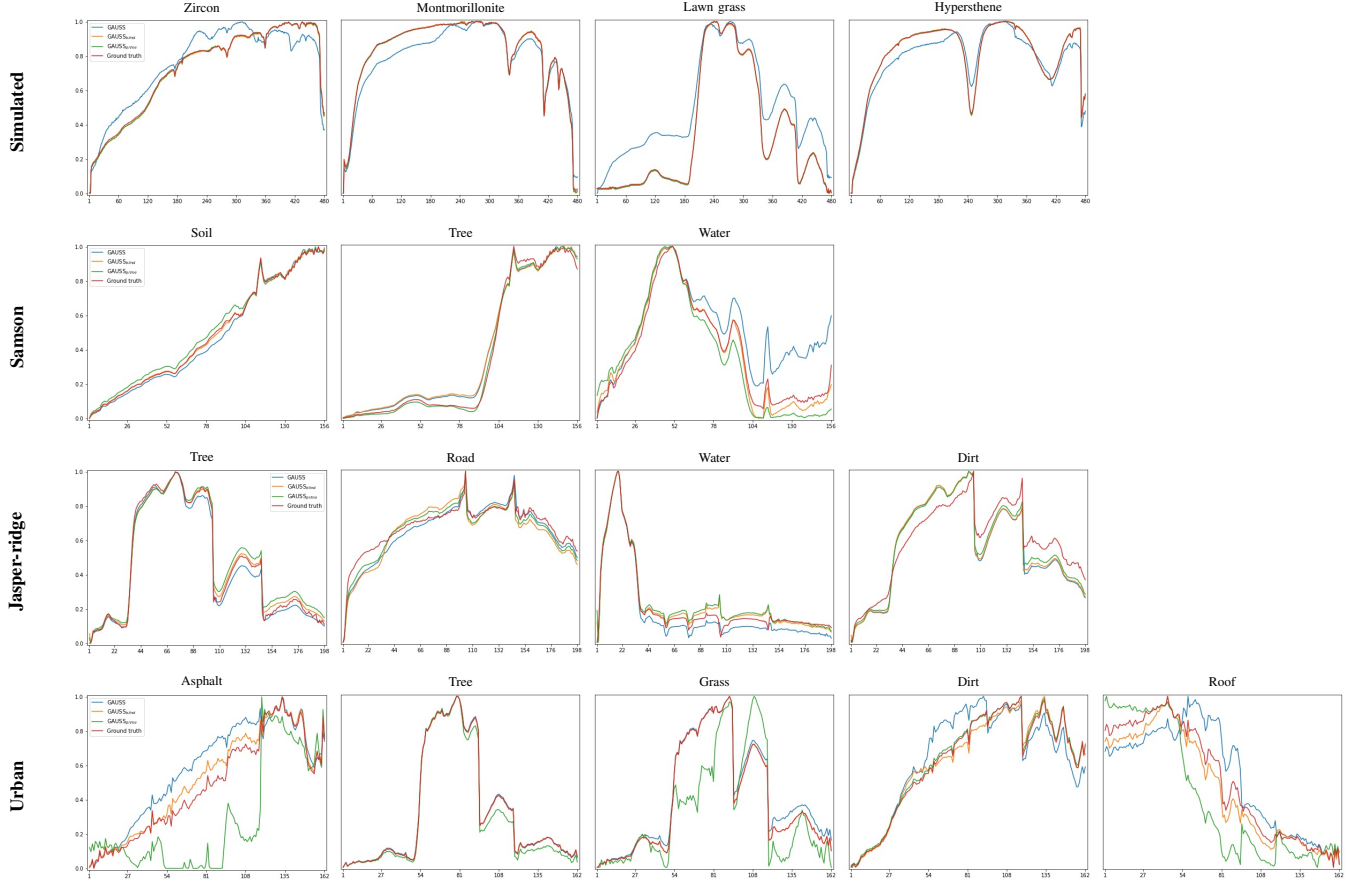


Fig. 5: Endmember signatures for the Simulated, Samson, Jasper-ridge, and Urban datasets for the proposed GAUSS, GAUSS<sub>blind</sub>, and GAUSS<sub>prime</sub> methods

maps of the GAUSS<sub>blind</sub> method. Moreover, using the  $L_{1/2}$  NMF abundances as the pseudo-ground truth, the GAUSS<sub>prime</sub> method has produced results better than the  $L_{1/2}$  NMF algorithm, similar to the simulated dataset. The reason is that the

network has benefited from both the GAUSS and  $L_{1/2}$  NMF method, which has learned different properties of the latent space of the HSI. Further, the fact that GAUSS<sub>prime</sub>, much like in the simulated dataset, continues to outperform both GAUSS and  $L_{1/2}$  NMF is clear evidence of optimal combining, and that it is better than the GAUSS<sub>blind</sub> is because reconstruction optimization is not as effective as  $L_{1/2}$  NMF steering here due to the specific landscape. Furthermore, there is no clear division in the performance between the conventional and DL unmixing algorithms for the Samson dataset according to Table II unlike for the simulated dataset. However, the cumulative error metrics of the conventional algorithms are lesser than that of the DL methods because the smaller endmember count and the sparsity in the HSI result in a simple geometry in the latent space, which is beneficial for the geometrical algorithms. This observation supports that using abundances from a conventional unsupervised algorithm as the pseudo-ground truth is feasible for HUA optimization. Besides that, in terms of endmember extraction performance, the DAEU has the best results by far, followed by the GAUSS<sub>prime</sub> method, but it has come at the expense of abundance performance. This trade-off between the abundance performance and endmember performance generally presents in both conventional and DL unmixing. Furthermore, the endmember performance of the GAUSS<sub>prime</sub> method has

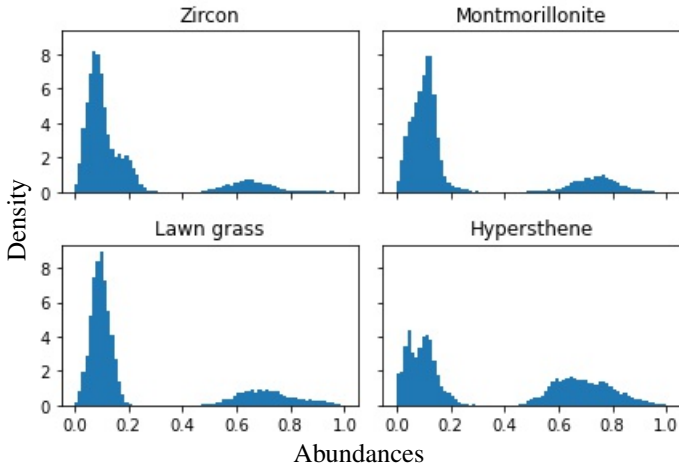


Fig. 6: Histogram of the abundance values for the ground truth of the simulated dataset



better results than that of the  $L_{1/2}$  NMF algorithm, which produced the pseudo-ground truths for the  $\text{GAUSS}_{\text{prime}}$  method. Therefore, as the  $\text{GAUSS}_{\text{prime}}$  method has outperformed  $L_{1/2}$  NMF algorithm in both abundance and endmember performance, the performance increment should be from combining the best attributes of the other two architectures. In addition, the performance boost, without the trade-off between abundance and endmember performances, from the GAUSS to  $\text{GAUSS}_{\text{prime}}$  method advocates the use of conventional unmixing algorithms as a supervisory input for AE, if and when applicable.

Consequently, the decoder of the  $\text{GAUSS}_{\text{prime}}$  method has benefited from using the AN in the HUA and the pseudo-ground truth from the  $L_{1/2}$  NMF algorithm. Since the AN improves the association between the neighbour pixels and the centre pixel, the sparsity in the HSI resulted from the direct impact of the  $L_{1/2}$  NMF algorithm will be complemented. As the output of the encoder is fed to the decoder and its output is compared against the pixels that promote sparsity in the image, the decoder benefits from the properties used by other unmixing algorithms. This combination of different aspects of algorithms via dedicated networks signifies the use of the AN and a pseudo-ground truth, as proposed in this work.

2) *Jasper-ridge dataset*: The Jasper-ridge dataset has four endmembers, and their boundaries are not as non-overlapping as in the simulated and the Samson dataset. Therefore, it is hard to expect sparsity in the abundance maps except for the water endmember. However, the UN has alleviated abundance binarization for dirt and tree endmembers. Nonetheless, the region identified by the encoder has been a success for water, road, and dirt. In contrast, the regions with lower abundances for the tree have not been identified under the GAUSS method. Despite binarization, the GAUSS method, as the parent method for both  $\text{GAUSS}_{\text{blind}}$  and  $\text{GAUSS}_{\text{prime}}$  methods, has produced competitive abundance estimation results while recording second-best error metrics for aAAD according to Table II. Moreover, this error performance indicates that larger quantities of binarization appear in the ground truth for abundances, hence the inherent spatial smoothness in the dataset captured by the AN.

The  $\text{GAUSS}_{\text{blind}}$  has produced the second-best performance for abundance estimation effortlessly, owing to the better performance of the GAUSS method. With the gradients of the reconstruction error, the UN has been able to span further the regions corresponding to lower or mixed abundances in the latent space. The reduction in aRMSE supports this idea as the aRMSE measures the distance between the estimated and the actual abundance values. Furthermore, the improvement in aAID is evidence that the variations in the abundance vectors of the estimated and the ground truth are textually similar, as aAID measures the similarity in the two probability vectors. Then, the  $\text{GAUSS}_{\text{prime}}$  method has the best abundance error metrics for the Jasper-ridge dataset. However, the pseudo-ground truth from the  $L_{1/2}$  NMF algorithm has worse abundance error metrics than the GAUSS method. Therefore, unlike with the previous datasets, superior performance has been achieved by the  $\text{GAUSS}_{\text{prime}}$  method than its predecessor despite using a contextually degraded pseudo-ground truth. The results can

explain the effect of the GAUSS method. The AN's spatial smoothness mechanic is now performing much more effectively in this landscape; hence the output of GAUSS has become much better and, in fact, better than SP methods like  $L_{1/2}$  NMF. However,  $\text{GAUSS}_{\text{prime}}$ , with its much superior pseudo-ground truth and the added effectiveness of the AN's spatial smoothing mechanic, has pivoted it further than both  $L_{1/2}$  NMF, GAUSS, and the rest. Here, the pseudo-ground truth from the  $L_{1/2}$  NMF abundances is considered superior to the more rudimentary one-hot encoded maps of the GAUSS method. Then, according to Table II, the GAUSS method has lower aAAD and the best error metrics for endmember extraction. The latter suggests that, as mentioned before, there are a large number of pure pixels in the HSI; hence, the decoder has been able to correctly estimate these endmembers better than any other algorithm in Table II. Since this suggests that the decoder is now at an optimal state, the reconstruction loss precluded the UN from degrading during the optimization of the encoder in the  $\text{GAUSS}_{\text{prime}}$  method. According to Fig. 4, the GAUSS method has information about pure or primarily pure abundances while the  $L_{1/2}$  NMF algorithm has information about lower abundances. Therefore, using the two pseudo-ground truths has complemented each other in the  $\text{GAUSS}_{\text{prime}}$  method, which reaffirms the benefits of using supervisory data to train the encoder, initially proposed for the GAUSS method with the k-means algorithm.

Then, in the Jasper-ridge dataset, the road endmember is challenging to extract since it is scarce compared to other endmembers and heavily correlates with the dirt endmember, despite having high reflectance values. As a result, most algorithms have not successfully extracted the road endmember, especially conventional algorithms and ultimately its abundance values. However, according to Fig. 5, all three methods in the proposed work have extracted a valid signature for the road while GAUSS method has had the highest success. This achievement was made possible by the AN and the pseudo-ground truth. Because the AN has managed to decorrelate the pure endmembers to conform to their high correlation, and as a result, the decoder has been allowed to extract the road endmember accurately as opposed to the comparative algorithms. Therefore, the endmember performance of the GAUSS method for the Jasper-ridge dataset signifies the contribution of the GAUSS method.

3) *Urban dataset*: The abundances maps' binarisation is also present for the urban dataset under the GAUSS method. Nevertheless, according to Table II, the GAUSS method has competitive results for the aAAD and aAID error metrics. Therefore, the actual ground truth abundances of the urban dataset are much closer to pure abundances to reconcile with the abundance estimation performance under the method. Furthermore, since the boundaries are non-overlapping, the network has managed to identify these boundaries of each endmember.

For the urban dataset, the  $\text{GAUSS}_{\text{blind}}$  method has produced the best results for estimating the abundance and endmembers while the GAUSS method has competitive results for abundance error metrics. However, even though the DAEU architecture is comparable with the  $\text{GAUSS}_{\text{blind}}$  method architecture, the performance of the DAEU is poor than that of the  $\text{GAUSS}_{\text{blind}}$

method. Since the GAUSS method performs unmixing pixel-wise, the benefits of the spatial features in the urban HSI should be extracted by AN, which feeds its output to the UN. Furthermore, given that aAAD value is much lower for the GAUSS method, the one-hot encoded abundance from k-means has been sufficiently accurate to train the UN of the HUA.

However, the performance has deteriorated from the GAUSS to GAUSS<sub>prime</sub> method in contrast to the other three datasets because the pseudo-ground truth from the  $L_{1/2}$  NMF algorithm has not been an accurate supervisory input for the UN. According to Table II,  $L_{1/2}$  NMF algorithm has far poorer results for abundance estimation than the GAUSS method. Also, the abundance maps for  $L_{1/2}$  NMF in Fig. 4 have much lower abundance values for most of the endmembers, and the maps have significantly deviated from the ground truths. Since there is a marked difference between the ground truth and the  $L_{1/2}$  NMF abundances, the UN has not been able to improve using a conventional algorithm with inferior performance like with the Jasper-ridge dataset. Nonetheless, it should be noted that the pseudo-ground truth of the GAUSS<sub>prime</sub> method could be any reliable SP algorithm, and the  $L_{1/2}$  NMF algorithm was used to maintain consistency among the datasets.

The GAUSS<sub>blind</sub> method has the best performance for end-member extraction, while the GAUSS method also produces competitive results. Therefore, the decoder for the GAUSS<sub>blind</sub> method has already been initiated around the decoder's optimal solution. According to the aSAD metric, the endmember performance is as improved as the abundance error metric. Hence, the proposed AN and the one-hot encoded pseudo-ground truth have been conducive for endmember estimation. Furthermore, the best performing error metrics for the urban dataset are shared amongst the same set of algorithms: GAUSS<sub>blind</sub>, CNNAEU, EGUnet, and GAUSS. Therefore, for the urban dataset, the better estimation of abundances has been beneficial for better endmember extraction.

4) *Training method selection:* This work discussed three variants for the HUA: GAUSS, GAUSS<sub>blind</sub>, and GAUSS<sub>prime</sub>. However, the three variants affected the unmixing results depending on the HS dataset. In general, the GAUSS<sub>prime</sub> method outperformed the other two methods except in the urban dataset, while the GAUSS<sub>blind</sub> method produced results comparable with that of the GAUSS<sub>prime</sub> method. Further, the initially proposed GAUSS method had better error metrics than existing HU methods and, in addition, produced better results than the GAUSS<sub>prime</sub> method for the urban dataset. Hence, it is pertinent to discuss selecting the best training strategy for an unseen dataset; as evidenced by the Urban dataset, it is beneficial to fix the secondary pseudo-ground truth to one method. For that, we suggest using the reconstruction error in 14 of the HSI. Accordingly, the reconstruction errors for the four experimental datasets under each method are tabulated in Table III.

According to Table III, the method with the least reconstruction error for each dataset has the best performing figures for unmixing results in Table II. Therefore, though the authors have chosen the  $L_{1/2}$  NMF algorithm as the conventional algorithm to construct a pseudo-ground truth for the training of the UN,

TABLE III  
Average reconstruction error for the experimental dataset under each training strategy

	Simulated	Samson	Jasper-ridge	Urban
GAUSS	0.02336	0.07887	0.07392	0.02731
GAUSS <sub>blind</sub>	0.02185	0.07581	0.05743	0.02094
GAUSS <sub>prime</sub>	0.02184	0.06601	0.05489	0.04324

the selection of a suitable unsupervised algorithm can also be based on the reconstruction error of the HSI for that algorithm. However, in this work, the  $L_{1/2}$  NMF algorithm was used to maintain the consistency in the comparison and remove the effect of using different algorithms in constructing the pseudo-ground truth.

## V. CONCLUSION

In this paper, we proposed three algorithms for HU. In this work, we discuss split training of the encoder-decoder with an additional network (AN) preceding the UN and the use of a pseudo-ground truth for abundances for supervised learning of the UN. Then, the AN approximates centre pixels from their neighbourhood to improve the association between nearby pixels and spatial correlation; and perform decorrelation of pixel and endmember impurities. In addition, the use of the pseudo-ground truth accelerated encoder training. It facilitated non-linear decoder architecture, emulating the mixing process in remote sensing and enabling subsequent training procedures with more refined abundance maps as pseudo-ground truths for improved performance. Using the pseudo-ground truth created with k-means segmentation resulted in abundance binarization, but it was conducive to estimating pure endmembers of the HSI. Besides that, we propose two variants for the initially proposed HUA, which resulted from the flexibility generated by the original GAUSS method. In the GAUSS<sub>blind</sub>, we combine the encoder and decoder to back-propagate the reconstruction error gradients to both the decoder and the encoder. Then, in the GAUSS<sub>prime</sub>, we experimented with using the abundance results of a SP-based unmixing method as the pseudo-ground truth with the combined encoder-decoder architecture, which was made possible due to the introduced pseudo-ground truth mechanic that decoupled and enabled such abundance steering. Subsequent variants mostly outperformed or produced results competitive with existing unmixing algorithms from DL and SP domains. Further, the initially proposed architecture produced competitive error metrics, and it is the main contributor to the superior performance of the other two variants that went a step further by combining this with other mechanics such as refined abundance optimization via secondary pseudo-ground truth training or backpropagation of reconstruction loss to both mixing and unmixing networks. Besides, we discussed the effect of the dataset on the performance of the unmixing method and the selection of the unmixing algorithm out of the proposed methods for an unseen hyperspectral dataset. Meanwhile, the same technique could be applied to deciding on an algorithm to create the pseudo-ground truth.

## REFERENCES

- [1] M. J. Khan, H. S. Khan, A. Yousaf, K. Khurshid, and A. Abbas, "Modern trends in hyperspectral image analysis: A review," *IEEE Access*, vol. 6, pp. 14 118–14 129, 2018.
- [2] L. Liu, J. Feng, L. Han, J. Zhou, X. Xu, and R. Liu, "Mineral mapping using spaceborne tiangong-1 hyperspectral imagery and aster data: A case study of alteration detection in support of regional geological survey at jintanzi-malianquan area, beishan, gansu province, china," *Geological Journal*, vol. 53, pp. 372–383, 2018.
- [3] S. Lorenz, M. Kirsch, R. Zimmermann, L. Tusa, R. Möckel, M. Chamberland, and R. Gloaguen, "Long-wave hyperspectral imaging for lithological mapping: A case study," in *IGARSS 2018-2018 IEEE International Geoscience and Remote Sensing Symposium*. IEEE, 2018, pp. 1620–1623.
- [4] F. A. Kruse, J. W. Boardman, and J. F. Huntington, "Comparison of airborne hyperspectral data and eo-1 hyperion for mineral mapping," *IEEE Transactions on Geoscience and Remote Sensing*, vol. 41, no. 6, pp. 1388–1400, 2003.
- [5] L. Ni, H. Xu, and X. Zhou, "Mineral identification and mapping by synthesis of hyperspectral vnir/swir and multispectral tir remotely sensed data with different classifiers," *IEEE Journal of Selected Topics in Applied Earth Observations and Remote Sensing*, vol. 13, pp. 3155–3163, 2020.
- [6] X. Chen, J. Chen, and J. Pan, "Sulfate mineral mapping with hyperspectral imagery, a case study of the rodalquilar area, se spain," in *2019 10th Workshop on Hyperspectral Imaging and Signal Processing: Evolution in Remote Sensing (WHISPERS)*. IEEE, 2019, pp. 1–5.
- [7] M. B. Stuart, A. J. McGonigle, and J. R. Willmott, "Hyperspectral imaging in environmental monitoring: a review of recent developments and technological advances in compact field deployable systems," *Sensors*, vol. 19, no. 14, p. 3071, 2019.
- [8] D. Zeng, S. Zhang, F. Chen, and Y. Wang, "Multi-scale cnn based garbage detection of airborne hyperspectral data," *IEEE Access*, vol. 7, pp. 104 514–104 527, 2019.
- [9] M. Moroni, E. Lupo, E. Marra, and A. Cenedese, "Hyperspectral image analysis in environmental monitoring: setup of a new tunable filter platform," *Procedia Environmental Sciences*, vol. 19, pp. 885–894, 2013.
- [10] B. Lu, P. D. Dao, J. Liu, Y. He, and J. Shang, "Recent advances of hyperspectral imaging technology and applications in agriculture," *Remote Sensing*, vol. 12, no. 16, p. 2659, 2020.
- [11] M. Zhu, D. Huang, X.-J. Hu, W.-H. Tong, B.-L. Han, J.-P. Tian, and H.-B. Luo, "Application of hyperspectral technology in detection of agricultural products and food: A review," *Food Science & Nutrition*, vol. 8, no. 10, pp. 5206–5214, 2020.
- [12] M. Teke, H. S. Deveci, O. Haliloğlu, S. Z. Gürbüz, and U. Sakarya, "A short survey of hyperspectral remote sensing applications in agriculture," in *2013 6th international conference on recent advances in space technologies (RAST)*. IEEE, 2013, pp. 171–176.
- [13] B. Rasti, P. Scheunders, P. Ghamisi, G. Licciardi, and J. Chanussot, "Noise reduction in hyperspectral imagery: Overview and application," *Remote Sensing*, vol. 10, no. 3, p. 482, 2018.
- [14] R. Heylen, M. Parente, and P. Gader, "A review of nonlinear hyperspectral unmixing methods," *IEEE Journal of Selected Topics in Applied Earth Observations and Remote Sensing*, vol. 7, no. 6, pp. 1844–1868, 2014.
- [15] N. Dobigeon, J.-Y. Tourneret, C. Richard, J. C. M. Bermudez, S. McLaughlin, and A. O. Hero, "Nonlinear unmixing of hyperspectral images: Models and algorithms," *IEEE Signal processing magazine*, vol. 31, no. 1, pp. 82–94, 2013.
- [16] A. Halimi, Y. Altmann, N. Dobigeon, and J.-Y. Tourneret, "Nonlinear unmixing of hyperspectral images using a generalized bilinear model," *IEEE Transactions on Geoscience and Remote Sensing*, vol. 49, no. 11, pp. 4153–4162, 2011.
- [17] J. Gu, B. Yang, and B. Wang, "Nonlinear unmixing for hyperspectral images via kernel-transformed bilinear mixing models," *IEEE Transactions on Geoscience and Remote Sensing*, 2021.
- [18] J. M. Bioucas-Dias, A. Plaza, N. Dobigeon, M. Parente, Q. Du, P. Gader, and J. Chanussot, "Hyperspectral unmixing overview: Geometrical, statistical, and sparse regression-based approaches," *IEEE journal of selected topics in applied earth observations and remote sensing*, vol. 5, no. 2, pp. 354–379, 2012.
- [19] J. M. Nascimento and J. M. Dias, "Vertex component analysis: A fast algorithm to unmix hyperspectral data," *IEEE Transactions on Geoscience and Remote Sensing*, vol. 43, no. 4, pp. 898–910, 2005.
- [20] J. Boardman, "Automating spectral unmixing of aviris data using convex geometry concepts. summaries of the 4th annual jpl airborne geosciences workshop," *Jet Propulsion Laboratory, Pasadena, California*, 1993.
- [21] M. E. Winter, "N-findr: An algorithm for fast autonomous spectral end-member determination in hyperspectral data," in *Imaging Spectrometry V*, vol. 3753. International Society for Optics and Photonics, 1999, pp. 266–275.
- [22] L. Miao and H. Qi, "Endmember extraction from highly mixed data using minimum volume constrained nonnegative matrix factorization," *IEEE Transactions on Geoscience and Remote Sensing*, vol. 45, no. 3, pp. 765–777, 2007.
- [23] A. Zare and P. Gader, "Sparsity promoting iterated constrained endmember detection in hyperspectral imagery," *IEEE Geoscience and Remote Sensing Letters*, vol. 4, no. 3, pp. 446–450, 2007.
- [24] P. Gader, D. Dranishnikov, A. Zare, and J. Chanussot, "A sparsity promoting bilinear unmixing model," in *2012 4th Workshop on Hyperspectral Image and Signal Processing: Evolution in Remote Sensing (WHISPERS)*. IEEE, 2012, pp. 1–4.
- [25] L. Zhuang, C.-H. Lin, M. A. Figueiredo, and J. M. Bioucas-Dias, "Regularization parameter selection in minimum volume hyperspectral unmixing," *IEEE Transactions on Geoscience and Remote Sensing*, vol. 57, no. 12, pp. 9858–9877, 2019.
- [26] J. Li, J. M. Bioucas-Dias, A. Plaza, and L. Liu, "Robust collaborative nonnegative matrix factorization for hyperspectral unmixing," *IEEE Transactions on Geoscience and Remote Sensing*, vol. 54, no. 10, pp. 6076–6090, 2016.
- [27] J. M. Bioucas-Dias, "A variable splitting augmented lagrangian approach to linear spectral unmixing," in *2009 First workshop on hyperspectral image and signal processing: Evolution in remote sensing*. IEEE, 2009, pp. 1–4.
- [28] L. Parra, C. Spence, P. Sajda, A. Ziehe, and K.-R. Müller, "Unmixing hyperspectral data," *Advances in neural information processing systems*, vol. 12, 1999.
- [29] N. Dobigeon, S. Moussaoui, M. Coulon, J.-Y. Tourneret, and A. O. Hero, "Joint bayesian endmember extraction and linear unmixing for hyperspectral imagery," *IEEE Transactions on Signal Processing*, vol. 57, no. 11, pp. 4355–4368, 2009.
- [30] J. M. Nascimento and J. M. Bioucas-Dias, "Hyperspectral unmixing algorithm via dependent component analysis," in *2007 IEEE International Geoscience and Remote Sensing Symposium*. IEEE, 2007, pp. 4033–4036.
- [31] J. M. Bioucas-Dias and M. A. Figueiredo, "Alternating direction algorithms for constrained sparse regression: Application to hyperspectral unmixing," in *2010 2nd Workshop on Hyperspectral Image and Signal Processing: Evolution in Remote Sensing*. IEEE, 2010, pp. 1–4.
- [32] M.-D. Iordache, J. M. Bioucas-Dias, and A. Plaza, "Total variation spatial regularization for sparse hyperspectral unmixing," *IEEE Transactions on Geoscience and Remote Sensing*, vol. 50, no. 11, pp. 4484–4502, 2012.
- [33] D. D. Lee and H. S. Seung, "Algorithms for non-negative matrix factorization," in *Advances in neural information processing systems*. MIT Press, 2000, p. 535–541.
- [34] Y. Qian, S. Jia, J. Zhou, and A. Robles-Kelly, "L1/2 sparsity constrained nonnegative matrix factorization for hyperspectral unmixing," in *2010 International conference on digital image computing: techniques and applications*. IEEE, 2010, pp. 447–453.
- [35] W. He, H. Zhang, and L. Zhang, "Total variation regularized reweighted sparse nonnegative matrix factorization for hyperspectral unmixing," *IEEE Transactions on Geoscience and Remote Sensing*, vol. 55, no. 7, pp. 3909–3921, 2017.
- [36] E. Ekanayake, H. Weerasooriya, D. Ranasinghe, S. Herath, B. Rathnayake, G. Godaliyadda, M. Ekanayake, and H. Herath, "Constrained nonnegative matrix factorization for blind hyperspectral unmixing incorporating end-member independence," *IEEE Journal of Selected Topics in Applied Earth Observations and Remote Sensing*, vol. 14, pp. 11 853–11 869, 2021.
- [37] X. Sun, Q. Peng, B. Zhang, L. Gao, and L. Yang, "Constraint non-negative matrix factorization with sparseness and piece wise smoothness for hyperspectral unmixing," in *2018 9th Workshop on Hyperspectral Image and Signal Processing: Evolution in Remote Sensing (WHISPERS)*. IEEE, 2018, pp. 1–5.
- [38] S. Yang, X. Zhang, Y. Yao, S. Cheng, and L. Jiao, "Geometric nonnegative matrix factorization (gnmf) for hyperspectral unmixing," *IEEE Journal of Selected Topics in Applied Earth Observations and Remote Sensing*, vol. 8, no. 6, pp. 2696–2703, 2015.
- [39] B. Rathnayake, E. Ekanayake, K. Weerakoon, G. Godaliyadda, M. Ekanayake, and H. Herath, "Graph-based blind hyperspectral unmixing via nonnegative matrix factorization," *IEEE Transactions on Geoscience and Remote Sensing*, vol. 58, no. 9, pp. 6391–6409, 2020.
- [40] L. Zhou, X. Zhang, J. Wang, X. Bai, L. Tong, L. Zhang, J. Zhou, and E. Hancock, "Subspace structure regularized nonnegative matrix

- factorization for hyperspectral unmixing,” *IEEE Journal of Selected Topics in Applied Earth Observations and Remote Sensing*, vol. 13, pp. 4257–4270, 2020.
- [41] A. Signoroni, M. Savardi, A. Baronio, and S. Benini, “Deep learning meets hyperspectral image analysis: A multidisciplinary review,” *Journal of Imaging*, vol. 5, no. 5, p. 52, 2019.
- [42] L. Qi, J. Li, Y. Wang, M. Lei, and X. Gao, “Deep spectral convolution network for hyperspectral image unmixing with spectral library,” *Signal Processing*, vol. 176, p. 107672, 2020.
- [43] X. Zhang, Y. Sun, J. Zhang, P. Wu, and L. Jiao, “Hyperspectral unmixing via deep convolutional neural networks,” *IEEE Geoscience and Remote Sensing Letters*, vol. 15, no. 11, pp. 1755–1759, 2018.
- [44] B. Palsson, M. O. Ulfarsson, and J. R. Sveinsson, “Convolutional autoencoder for spectral–spatial hyperspectral unmixing,” *IEEE Transactions on Geoscience and Remote Sensing*, vol. 59, no. 1, pp. 535–549, 2020.
- [45] Y. Ranasinghe, S. Herath, K. Weerasooriya, M. Ekanayake, R. Godaliyadda, P. Ekanayake, and V. Herath, “Convolutional autoencoder for blind hyperspectral image unmixing,” in *2020 IEEE 15th International Conference on Industrial and Information Systems (ICIIS)*. IEEE, 2020, pp. 174–179.
- [46] M. Wang, M. Zhao, J. Chen, and S. Rahardja, “Nonlinear unmixing of hyperspectral data via deep autoencoder networks,” *IEEE Geoscience and Remote Sensing Letters*, vol. 16, no. 9, pp. 1467–1471, 2019.
- [47] M. Zhao, M. Wang, J. Chen, and S. Rahardja, “Hyperspectral unmixing for additive nonlinear models with a 3-d-cnn autoencoder network,” *IEEE Transactions on Geoscience and Remote Sensing*, 2021.
- [48] M. Zhao, S. Shi, J. Chen, and N. Dobigeon, “A 3d-cnn framework for hyperspectral unmixing with spectral variability,” *IEEE Transactions on Geoscience and Remote Sensing*, 2022.
- [49] Y. Fang, Y. Wang, L. Xu, R. Zhuo, A. Wong, and D. A. Clausi, “Bcun: Bayesian fully convolutional neural network for hyperspectral spectral unmixing,” *IEEE Transactions on Geoscience and Remote Sensing*, pp. 1–1, 2022.
- [50] S. Ozkan, B. Kaya, and G. B. Akar, “Endnet: Sparse autoencoder network for endmember extraction and hyperspectral unmixing,” *IEEE Transactions on Geoscience and Remote Sensing*, vol. 57, no. 1, pp. 482–496, 2018.
- [51] Y. Qu and H. Qi, “udas: An untied denoising autoencoder with sparsity for spectral unmixing,” *IEEE Transactions on Geoscience and Remote Sensing*, vol. 57, no. 3, pp. 1698–1712, 2018.
- [52] Y. Su, J. Li, A. Plaza, A. Marinoni, P. Gamba, and S. Chakravorty, “Daen: Deep autoencoder networks for hyperspectral unmixing,” *IEEE Transactions on Geoscience and Remote Sensing*, vol. 57, no. 7, pp. 4309–4321, 2019.
- [53] Z. Han, D. Hong, L. Gao, B. Zhang, and J. Chanussot, “Deep half-siamese networks for hyperspectral unmixing,” *IEEE Geoscience and Remote Sensing Letters*, vol. 18, no. 11, pp. 1996–2000, 2020.
- [54] D. Hong, L. Gao, J. Yao, N. Yokoya, J. Chanussot, U. Heiden, and B. Zhang, “Endmember-guided unmixing network (egu-net): A general deep learning framework for self-supervised hyperspectral unmixing,” *IEEE Transactions on Neural Networks and Learning Systems*, 2021.
- [55] M. Zhao, L. Yan, and J. Chen, “Lstm-dnn based autoencoder network for nonlinear hyperspectral image unmixing,” *IEEE Journal of Selected Topics in Signal Processing*, vol. 15, no. 2, pp. 295–309, 2021.
- [56] B. Palsson, M. O. Ulfarsson, and J. R. Sveinsson, “Convolutional autoencoder for spatial-spectral hyperspectral unmixing,” in *IGARSS 2019-2019 IEEE International Geoscience and Remote Sensing Symposium*. IEEE, 2019, pp. 357–360.
- [57] B. Palsson, J. Sigurdsson, J. R. Sveinsson, and M. O. Ulfarsson, “Hyperspectral unmixing using a neural network autoencoder,” *IEEE Access*, vol. 6, pp. 25 646–25 656, 2018.
- [58] Y. Ranasinghe, S. Herath, K. Weerasooriya, M. Ekanayake, R. Godaliyadda, P. Ekanayake, and V. Herath, “Convolutional autoencoder for blind hyperspectral image unmixing,” in *2020 IEEE 15th International Conference on Industrial and Information Systems (ICIIS)*, 2020, pp. 174–179.
- [59] H. Li, R. A. Borsoi, T. Imbiriba, P. Closas, J. C. M. Bermudez, and D. Erdoğmuş, “Model-based deep autoencoder networks for nonlinear hyperspectral unmixing,” *IEEE Geoscience and Remote Sensing Letters*, vol. 19, pp. 1–5, 2022.
- [60] K. T. Shahid and I. D. Schizas, “Unsupervised hyperspectral unmixing via nonlinear autoencoders,” *IEEE Transactions on Geoscience and Remote Sensing*, vol. 60, pp. 1–13, 2022.
- [61] N. Dobigeon, Y. Altmann, N. Brun, and S. Moussaoui, “Linear and nonlinear unmixing in hyperspectral imaging,” in *Data Handling in Science and Technology*. Elsevier, 2016, vol. 30, pp. 185–224.
- [62] C.-I. Chang, “Spectral information divergence for hyperspectral image analysis,” in *IEEE 1999 International Geoscience and Remote Sensing Symposium. IGARSS’99 (Cat. No. 99CH36293)*, vol. 1. IEEE, 1999, pp. 509–511.
- [63] R. F. Kokaly, R. N. Clark, G. A. Swayze, K. E. Livo, T. M. Hoefen, N. C. Pearson, R. A. Wise, W. M. Benz, H. A. Lowers, R. L. Driscoll, and A. J. Klein, “USGS Spectral Library Version 7,” U.S. Geological Survey, Reston, VA, Report 1035, 2017. [Online]. Available: <http://pubs.er.usgs.gov/publication/ds1035>
- [64] D. Hong, L. Gao, J. Yao, N. Yokoya, J. Chanussot, U. Heiden, and B. Zhang, “Endmember-guided unmixing network (egu-net): A general deep learning framework for self-supervised hyperspectral unmixing,” *IEEE Transactions on Neural Networks and Learning Systems*, pp. 1–14, 2021.
- [65] R. Rajabi and H. Ghassemian, “Spectral unmixing of hyperspectral imagery using multilayer nmf,” *IEEE Geoscience and Remote Sensing Letters*, vol. 12, no. 1, pp. 38–42, 2014.
- [66] D. Hong and X. X. Zhu, “Sulora: Subspace unmixing with low-rank attribute embedding for hyperspectral data analysis,” *IEEE Journal of Selected Topics in Signal Processing*, vol. 12, no. 6, pp. 1351–1363, 2018.



**D.Y.L. Ranasinghe** received the B.Sc. (Eng.) degree in electrical and electronic engineering from the University of Peradeniya, Sri Lanka, in 2020. Immediately after that, he joined the School of Engineering, Sri Lanka Technological Campus, Padukka, Sri Lanka, as a Research Assistant. He is currently working as a Research Assistant with the University of Peradeniya under a research grant from the International Development Research Centre (IDRC), Canada. He has published in IEEE JSTARS, IEEE Access, and numerous IEEE conferences. His research interests

include hyperspectral and multispectral imaging, remote sensing, signal and image processing, and deep learning.



**H.M.H.K. Weerasooriya** received the B.Sc. degree in electrical and electronic engineering with a first-class honors from the University of Peradeniya, Peradeniya, Sri Lanka in 2020. He is currently an Instructor with the Department of Electronic and Electrical Engineering, University of Peradeniya. He is presently involved in the researches on hyperspectral imaging for remote sensing and agriculture applications, and he has numerous publications in IEEE conferences. His research interests include image processing, signal processing, communication, machine learning and deep learning.



**G.M.R.I. Godaliyadda** (Senior Member, IEEE) obtained his B.Sc. Engineering degree in Electrical and Electronic Engineering from the University of Peradeniya, Sri Lanka, in 2005, and Ph.D. from the National University of Singapore in 2011. Currently, he is attached to the University of Peradeniya, Faculty of Engineering, Department of Electrical and Electronic Engineering as a Senior Lecturer. His current research interests include image and signal processing, pattern recognition, computer vision, machine learning, smart grid, bio-medical and remote sensing applications and algorithms. He is a Senior Member of the IEEE. He is a recipient of the Sri Lanka President’s Award for Scientific Publications for 2018 and 2019. He is the recipient of multiple grants through the National Science Foundation (NSF) for research activities. His previous works have been published in IEEE-TGRS and several other IEEE-GRSS conferences including WHISPERS and IGARSS. He also has numerous publications in many other IEEE transactions, Elsevier and IET journals and is the recipient of multiple best paper awards from international conferences for his work.



**H.M.V.R. Herath** (Senior Member, IEEE) received the B.Sc.Eng. degree in electrical and electronic engineering with 1st class honours from the University of Peradeniya, Peradeniya, Sri Lanka, in 1998, M.Sc. degree in electrical and computer engineering with the award of academic merit from the University of Miami, USA in 2002, and Ph.D. degree in electrical engineering from the University of Paderborn, Germany in 2009. In 2009, he joined the Department of Electrical and Electronic Engineering, University of Peradeniya, as a Senior Lecturer. His current research

interests include hyperspectral imaging for remote sensing, multispectral imaging for food quality assessment, Coherent optical communications and integrated electronics. Prof. Herath was a member of one of the teams that for the first time successfully demonstrated coherent optical transmission with QPSK and polarization multiplexing. He is a member of the Institution of Engineers, Sri Lanka and The Optical Society. He is a Senior Member of the IEEE. He was the General Chair of the IEEE International Conference on Industrial and Information Systems (ICIIS) 2013 held in Kandy, Sri Lanka. His previous works have been published in IEEE-TGRS and several other IEEE-GRSS conferences including WHISPERS and IGARSS. He received the paper award in the ICTer 2017 conference held in Colombo Sri Lanka. Prof. Herath is a recipient of Sri Lanka President's Award for scientific research in 2013.



**M.P.B. Ekanayake** (Senior Member, IEEE) received his B.Sc. Engineering degree in Electrical and Electronic Engineering from University of Peradeniya, Sri Lanka, in 2006, and Ph.D. from Texas Tech University in 2011. Currently, he is attached to the University of Peradeniya as a Senior Lecturer. His current research interests include applications of signal processing and system modeling in remote sensing, hyperspectral imaging, and smart grid. He is a Senior Member of the IEEE. He is a recipient of the Sri Lanka President's Award for Scientific Publications in 2018 and 2019.

He has obtained several grants through the National Science Foundation (NSF) for research projects. His previous works have been published in IEEE-TGRS and several other IEEE-GRSS conferences including WHISPERS and IGARSS. He also has multiple publications in many IEEE transactions, Elsevier and IET journals and has been awarded several best paper awards in international conferences.



**D. Jayasundara** received a first-class honors degree in Electrical and Electronic Engineering from University of Peradeniya (2021). He's currently working as an instructor at Department of Engineering Mathematics. His research interests include Mathematics, Deep Learning, Digital Communication and Signal Processing. At present, he is involved in research associated with Hyper-Spectral Imaging for Remote sensing and Applications of Multi-Spectral Imaging.



**L. Ramanayake** graduated with a second-class honors (upper division) degree in Electrical and Electronic Engineering from University of Peradeniya (2021). His research interest includes Machine Learning, Spectral Imaging, High Voltage Engineering and Signal Processing. Currently, he is involved in research associated with Hyper-Spectral Imaging for Identification of Probable Mineral Deposits and Application of Multi-spectral Imaging.



**N. Senarath** received a second-class honors degree in Electrical and Electronic Engineering from University of Peradeniya (2021). He's currently working as an instructor at Department of Engineering Mathematics. His research interests include Mathematics, Deep Learning, Digital Communication and Signal Processing. At present, he is involved in research associated with Hyper-Spectral Imaging for Remote sensing and Applications of Multi-Spectral Imaging.



**D. Wickramasinghe**, graduated with a second-class honors (upper division) degree in Electrical and Electronic Engineering University of Peradeniya (2021). His research interests include Machine Learning, Multi-Spectral Imaging and Signal Processing. Currently he is involved in researches related to Hyper-Spectral Imaging for Identification of Probable Mineral Deposits, Potable Water Quality Parameter assessing and Identifying Sugar Adulteration in Black Tea through Multispectral Imaging.